Monolithic co-aerogels of carbon/titanium dioxide as three dimensional nanostructured electrodes for energy storage

Sungwoo Yang [a], Yue Cai [a], Yingwen Cheng [a], C.V. Varanasi [b], Jie Liu [a],*

[a] Department of Chemistry, Duke University, Durham, NC 27708, USA
[b] Army Research Office, Research Triangle Park, NC 27709, USA

HIGHLIGHTS

► We developed a simple one-pot method for the synthesis of co-gel of carbon and TiO_2.
► The co-aerogel of carbon and TiO_2 demonstrated superior electrochemical properties for Li battery.
► We demonstrated the existence of interconnected carbon and metal oxide network in the co-aerogel structures.

ARTICLE INFO

ABSTRACT

Conductive fillers, such as amorphous carbon, carbon nanotube and graphene etc., are generally mixed with nanostructured metal oxide materials to improve the performance of electrode materials in energy storage devices. However, the conductive framework that provides path for electric conduction does not normally form a well-connected and robust 3-D network to ensure optimized ions transport. Here, we report a convenient, inexpensive and scalable method for synthesizing hybrid carbon and titanium dioxide co-gels and co-aerogels to improve the electrochemical capacity by combining both the lithium insertion and the surface storage mechanisms in Li ion batteries (LIBs) anodes. A monolithic piece of a hybrid C/TiO_2 co-aerogel can be directly used as an active electrode without the addition of binders, such as polyvinylidene fluoride (PVDF). As a result, the performance of LIB anodes using the hybrid co-aerogel is significantly improved over current LIBs based on carbon/titanium oxide composites. The reversible discharge capacity was stabilized at ~400 mAh g^{-1} at a 168 mA g^{-1} scan rate and an operating voltage between 3.0 and 0.05 V vs. Li^+/Li with excellent cyclic capacity retention. This approach, however, is not limited to only C/TiO_2 system but can be extended to other metal oxides to form co-gels with carbon to improve their potential use in numerous electrochemical, photocatalytic, and photoelectronic devices.

1. Introduction

Energy storage devices with high energy densities at high charging and discharging rate are still the main challenge in developing future electric vehicles (EV). Among all possible solutions, innovative electrode materials with architecturally tailored nanostructures have potential to enable revolutionary advances in energy storage devices [1]. Nanostructured electrode materials have remarkable advantages over the bulk electrode materials, such as the reduced diffusion length of ions, high surface area, and the buffering effect on stresses associated with the lithium ion intercalation/deintercalation process [2]. However, most nanostructured electroactive materials still have disadvantages due to their intrinsic material properties, such as low conductivities [3,4], slow mass transport [5,6], poor cycleability [7], and weak mechanical strength etc [8]. To overcome these problems, researchers proposed a conceptually ideal three dimensional (3-D) heterogeneous nanostructured electrode for future generation batteries [9]. This proposed future 3-D electrode possesses well-ordered 3-D interconnected pores and a well ordered 3-D interconnected electroactive nanomaterial with a conformal conductive coating layer to insure faster ion and electron transports with sufficient the mechanical strength. Several attempts have been made to obtain such well-ordered 3-D nanostructured electrodes [10–15]. However, these previous methods are at an early stage of scientific study. Methods that are practical for industry scale applications are yet to be developed. Here, we report a convenient one-pot synthesis method to obtain interpenetrating 3-D

---

* Corresponding author. Tel.: +1 919 660 1549; fax: +1 919 660 1605.
E-mail address: j.liu@duke.edu (J. Liu).

nanostructured metal oxide and carbon aerogel composite electrodes that offer improved electrochemical properties for energy storage applications by combining both the lithium insertion and the surface storage mechanisms in Li ion batteries (LIBs) anodes.

In our approach, we have combined advantages of three different concepts: the high surface area and controlled porosity of aerogels, the nanostructured metal oxide materials for their electrochemical properties, and the high electron transport properties of carbon materials. Aerogels have potential to exhibit very high power density due to their enormous interfacial surface area [16,17]. Various transition metal oxide aerogels can be synthesized by the sol−gel process. In fact, transition metal oxides of novel morphologies have been investigated as attractive active materials for rechargeable lithium-ion batteries (LIBs) [18,19]. Nanostructured transition metal oxides, such as SnO_2, Fe_2O_3, NiO, Co_3O_4, VO_x, MnO_x and TiO_2 [20–23], stimulated extensive research interest for LIBs [24]. However, there are disadvantages of using transition metal oxide alone as active electrodes. Their electrical conductivity is not high enough for fast charge transport, and their mechanical strength is not strong enough resulting in reducing the cyclic capacity. In order to resolve these disadvantages, researchers have incorporated carbon based materials, such as carbon nanotubes and graphene, in these metal oxide materials and have demonstrated significant improvements in the performance of these materials [25–29]. TiO_2 has been extensively studied as a prospective material for a variety of applications such as catalysis [30], photovoltaics [31], and sensing [32]. Among these applications, TiO_2 shows great potential as an anode electrode of lithium ion batteries (LIBs) [33] due to inherent protection against lithium deposition [34], low cost, low toxicity, and the ability to be fabricated as a nanomaterial delivering faster lithium insertion/desertion [2]. However, like many other metal oxide materials, its capacity has been limited by low electron transport [35]. In order to solve this problem, by direct growth of uniform anatase TiO_2 nanospheres on graphene sheets, Li et al. and Ding et al. demonstrated substantial improvement in lithium specific capacity [36–39], indicating a great potential for the material if the electron transport can be improved.

Here, we synthesized hybrid carbon and titanium dioxide (C/TiO_2) co-gels and co-aerogels, as 3-D nanostructured electrodes. The monolith of the hybrid C/TiO_2 co-aerogel (hereafter "the hybrid co-aerogel") can be directly used as active electrodes without the addition of binders, such as polyvinylidene fluoride (PVDF), or additives, such as carbon black. As a result, the performance of LIB anodes using the hybrid co-aerogel is significantly improved over anodes based on carbon/titanium oxide composite. Previously, hybrid C/TiO_2 composites have been synthesized by either dropcasting the Ti precursor solution on the carbon aerogel platform, or addition of polymer precursor solution to the Ti precursor solution (or vice versa) [40–45]. However, the structure of the hybrid gels was not fully characterized and the consequences of the co-aerogel structure on the properties related to energy storage were not studied.

Compared to earlier studies, the approach discussed here has many advantages, including: (1) low cost. The starting materials used in our approach are low cost chemicals compare to carbon nanotubes; (2) scalable. The process can be scaled to industry scale without much engineering challenges; (3) High uniformity of the composites as the co-aerogel materials are composed of interpenetrating nanoscale networks of metal oxide and carbon. The overall uniformity of the composite is achieved by starting with precursors uniformly mixed at molecular level. (4) The 3-D interconnected metal oxides with small diameter enhance surface storage mechanism (pseudo-capacities) as well as the conventional lithium insertion mechanism resulting in the superior lithium storage capability even at high scan rate. (5) Mechanical stability. The carbon aerogel helps the metal oxide to be mechanically stronger for high stability in charging/discharging cycles; (6) low internal resistance. The carbon network is well connected compare to the composites obtained by physical mixing of carbon and metal oxides. We believe these advantages will make the approach generally adapted by researchers and industry for future energy storage applications.

2. Result and discussion

2.1. Hybrid C/TiO_2 co-gel and co-aerogel

Both carbon aerogel and TiO_2 aerogels have been studied by many research groups before [46–48]. The mechanism of the gelation and the effect of pH, ageing time, temperature for pyrolytic transformation from polymer to carbon etc. can be found in many recent reports and reviews [46,48]. The preparation of carbon aerogel includes steps of polymerization of precursors, usually resorcinol (R) and formaldehyde (F), ageing, solvent exchange, supercritical drying, and pyrolysis of the organic aerogel at high temperature under inert environment. On the other hand, the formation of TiO_2 aerogel normally includes the gelation of titanium isopropoxide (TiO_2) in alcohol mixed with acidic aqueous solutions, ageing, solvent exchange, and supercritical drying. The gelation and post processing conditions are not always compatible for different gel systems, especially between inorganic and organic gels. Here, we have developed a one-pot process for the formation of TiO_2 and Resorcinol−Formaldehyde (RF) co-gels by controlling the gelation of both TiO_2 and RF polymer. The choice of solvent, catalysis for RF gelation, and adjusting sol−gel pH were found to be critical factors to synthesize the hybrid co-gels. (1) Water has been a conventional solvent for RF gelation. However, TiO_2 gelation is not compatible with high concentration of water due to its uncontrollable gelation rate in water. Therefore, ethanol was selected as solvent system for the hybrid co-aerogel, because both titanium dioxides precursor (titanium isopropoxide) and RF precursor (resorcinol and formaldehyde) can be effortlessly dissolved in ethanol. (2) Na_2CO_3 has been usually used as a catalyst, which is associated with the ability of CO_3^{2-} species to initiate the RF-polymerization reaction. However, the solubility of Na_2CO_3 is extremely poor in ethanol compared to water. To solve this problem, Na_2CO_3 and resorcinol were dissolved separately in formaldehyde solution (37 wt% in water) and ethanol, respectively before mixing the two. This small amount of water is found to be not destructive for the gelation process of TiO_2 aerogel. (3) The rate of hydrolysis and gelation of TiO_2 is strongly dependent on pH. As shown in Fig. S2, clear uniform TiO_2 gels were able to be prepared only below pH = 0.77 because lower pH decreases the rate of alcoxolation and oxolation reactions. Therefore, the pH of the RF sol has to be adjusted by adding diluted HCl solution (1.5 M) before it was mixed with the TiO_2 sol. Uniform hybrid RF/TiO_2 gels were found only with pH between 1.08 and 1.39. Lower pH inhibits the gelation of TiO_2, while higher pH accelerates the rate of hydrolysis and gelation of TiO_2. Fig. 1 illustrates the synthesis procedures for pure TiO_2 aerogel, the RF/TiO_2 co-aerogel and pure RF aerogel. Further details on the synthesis can be found in the experimental section.

Fig. 1a shows the three samples in sol stage, and the transparency of the hybrid RF/TiO_2 sol indicates the homogeneous mixture of TiO_2 sol and RF sol. The TiO_2 sol and hybrid RF/TiO_2 sol became gels within 30 min at room temperature, which is attributed to the TiO_2 gelation in both cases, but no gelation occurred in the carbon sol as expected. Then, all of these samples were placed in an oven at 70 °C for 6 h, and the carbon sol became a gel after
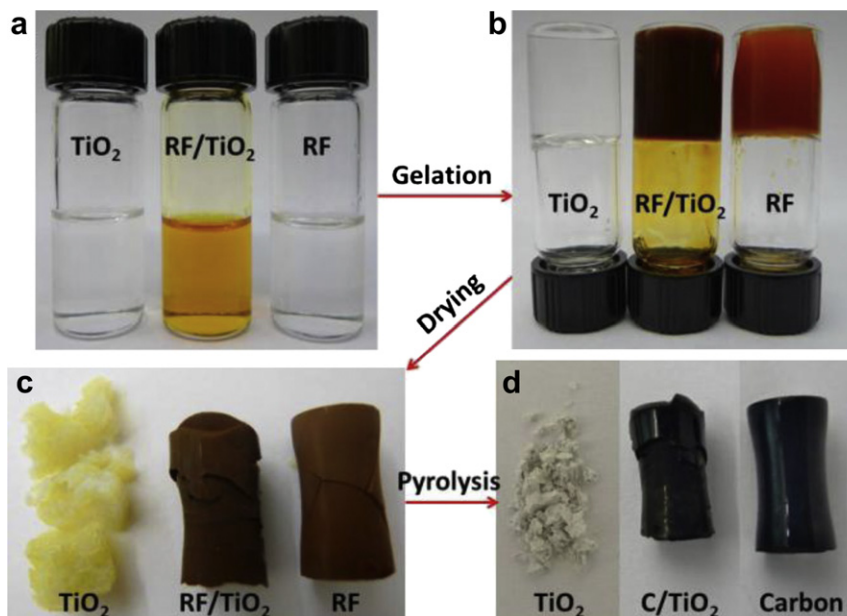
Fig. 1. (a) Images of TiO$_2$, hybrid and resorcinol/formaldehyde (R/F) gels (b) Images of TiO$_2$, hybrid and RF gels after gelation (c) images of TiO$_2$, hybrid and RF aerogels after critical point drying (CPD) process (d) images of TiO$_2$, hybrid and carbon aero-gels after pyrolysis at 900 °C for 5 h.

heat treatment as shown in Fig. 1b. These three gels were dried by the critical point dryer (CPD) process using CO$_2$, and Fig. 1c shows these three gels after the drying process. The hybrid co-gel and RF gel retained their shapes after CPD drying, but the pure TiO$_2$ gel was found to be brittle. The three dried gels were annealed at 900 °C for 5 h in an inert atmosphere for a pyrolytic transformation. Fig. 1d shows the final TiO$_2$, hybrid and carbon aerogels after carbonization. Interestingly, the hybrid co-aerogel retained its shape due to increase of its mechanical strength attributed by carbon component in the hybrid co-aerogel.

2.2. Morphology and structural characterization

A key question regarding the structure of the co-aerogel materials is whether the TiO$_2$ and C networks in the aerogel are well-linked or not. In order to prove that we have obtained a composite aerogel with interpenetrating carbon and TiO$_2$ networks, we have treated the co-aerogels under different conditions to remove one component at a time. Fig. 2 shows the hybrid co-aerogels before (Fig. 2a) and after air oxidation (Fig. 2b) at 500 °C for 1 h to remove carbon component and hydrofluoric acid (HF)

treatment (Fig. 2c) to remove TiO$_2$ component from the hybrid co-aerogel. One important aspect of the hybrid co-aerogel is uniformity, which can be achieved by co-gelation of carbon and TiO$_2$ sol. It is worthwhile noting that, after air oxidation and HF treatment, both TiO$_2$ and carbon aerogels remained as a monolith, indicating that both TiO$_2$ and carbon components possess 3-dimensional (3-D) interconnected random nanostructures in the hybrid co-aerogels, which is also demonstrated by TEM and SEM images in Fig. 3a and b, Figure S1 and S5 in the supporting information.

A closer observation by Transmission electron microscopy (TEM) in Fig. 3a and Figure S5 in supporting information indicates the homogeneous mixture of crystalline TiO$_2$ NPs and carbon. Because the dried hybrid co-gels were annealed at 900 °C for 5 h, titanium carbide (TiC) could have been produced during this treatment. However, Fig. 3c shows the X-ray photoelectron spectroscopy (XPS) emission of Carbon (1s) and Titanium (2p) of the hybrid co-aerogels. It indicates that no titanium carbide peaks were found in the C (1s) and Ti (2p) regions because the Ti 2p (3/2) binding energy for the carbide is around 454.9–455.1 eV while the C 1s peak for the carbide is around 281.7–281.9 eV [49–51]. The phase of TiO$_2$ is one critical aspect in the Li$^+$ insertion/desertion
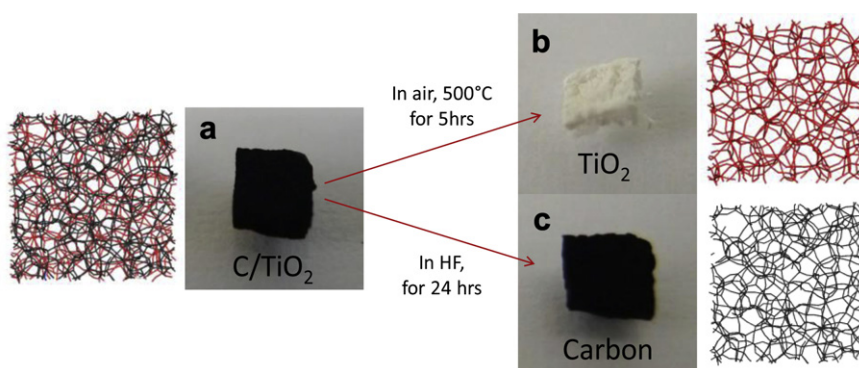
Fig. 2. (a) The hybrid co-aerogel and its visualized image (b) TiO$_2$ aerogel after removing carbon component by air oxidation at 500 °C for 5 h (c) carbon aerogel after removing TiO$_2$ component by HF treatment for 24 h with related visualized images.
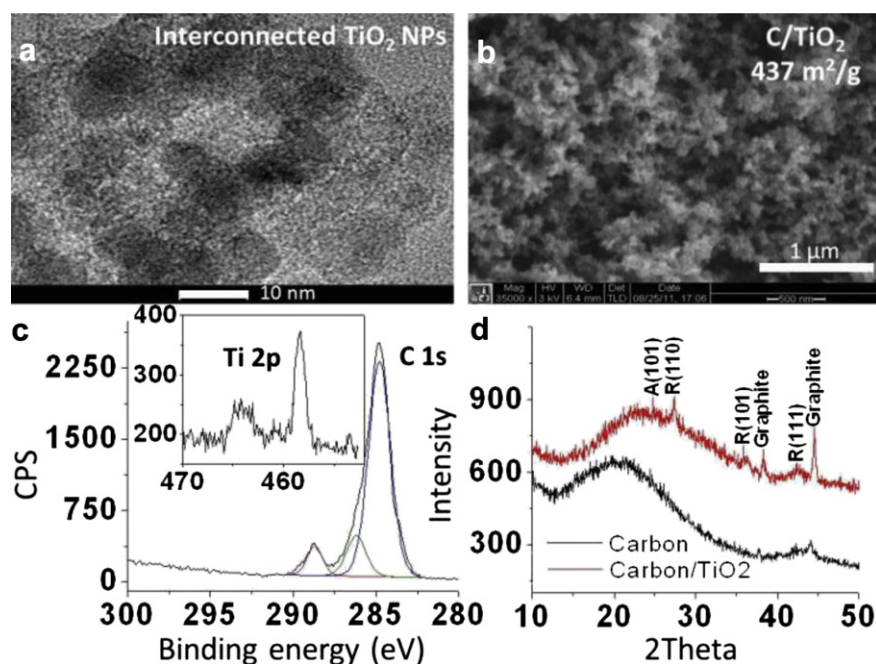
Fig. 3. (a) TEM (b) SEM (c) XPS and (d) XRD of the hybrid co-aerogel.

rate [52]. Fig 3d shows the X-ray diffraction (XRD) pattern of the hybrid co-aerogel. Rutile phase was found to present as a major phase of TiO_2, and graphite peaks were also found together as expected. In addition, thermal gravimetric analysis (TGA) in Figure S3 shows that the hybrid co-aerogel is composed of 58.2 wt% of TiO_2 and 41.8 wt% of carbon.

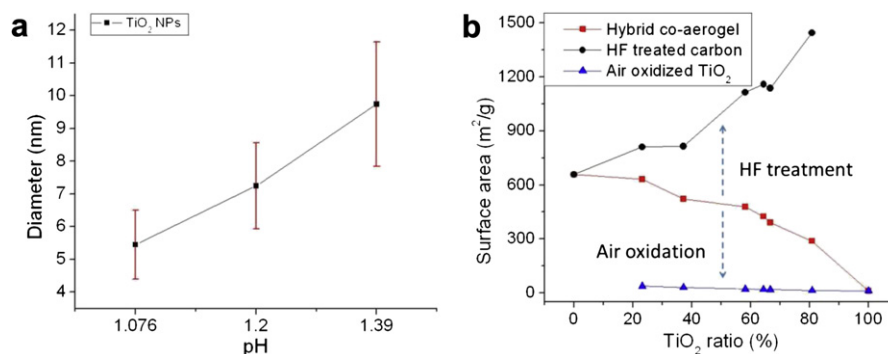The diameter of TiO_2 nanoparticles (NPs) in the hybrid co-aerogels can be controlled by adjusting the sol–gel pH. The average TiO_2 NPs' size increased with increased sol–gel pH as shown in Fig. 4a. For example, pH 1.08 had the smallest average TiO_2 NP size at 5.5 ± 1.0 nm, which was followed by an increase to 7.2 ± 1.3 nm and 9.7 ± 1.9 nm in samples prepared at pH 1.20 and 1.39 respectively. It was found that the higher sol–gel pH showed the larger standard deviation of NPs' diameter. This trend of increased TiO_2 NPs size with increased synthetic pH is consistent with previous reports [53]. The correlation between the total Brunauer–Emmett–Teller (BET) surface area of the hybrid co-aerogel and TiO_2 weight ratio (%) is presented in Fig. 4b (red line). The total surface area decreased with increasing TiO_2 contents. The weight ratio between TiO_2 and carbon can be easily controlled by changing the mixing volume ratio between the carbon precursor solution (RF solution) and the TiO_2 precursor solution (Ti solution) as described in the experimental section below. Notably, the surface area of a hybrid co-aerogel composed with 80 wt% TiO_2 is around 300 m^2 g^{-1}, which is well above that of conventional TiO_2 NPs ($\sim$50 m^2 g^{-1}). More importantly, it is worthwhile noting that the BET surface area of the HF-treated carbon aerogel (black line) was found to be higher than that of the reference carbon aerogel ($\sim$657 m^2 g^{-1}) which was prepared at the same sol–gel pH of the hybrid co-aerogel. Taking the hybrid co-aerogels containing 58.2 wt% of TiO_2 as an example, its total BET surface area was initially 478 m^2 g^{-1}. However, after removing TiO_2 components by HF treatment, the BET surface area of HF treated carbon aerogel was 915 m^2 g^{-1}. The HF treated carbon aerogels always show higher BET surface area than that of the reference carbon aerogel, as shown in Fig. 4b. In addition, the higher the TiO_2 contents in the hybrid co-aerogel, the higher the BET surface area in the HF treatment carbon aerogel. This trend might indicate that the

TiO_2 network is wrapped by the carbon network because TiO_2 gelation occurs first (within 30 min at room temperature) followed by RF gelation (around 6 h at 70 °C). In addition, XPS and energy-dispersive X-ray spectroscopy (EDS) analyses in Figure S4 also support this proposed structure. This structure is close to the proposed ideal 3D battery electrode structure by Lee et al. [9].

2.3. Monolithic lithium ion battery performance

To demonstrate advantages of the hybrid co-aerogels, a galvanostatic charge–discharge test was used to study their lithium insertion/desertion properties. Monolithic hybrid co-aerogel and the reference monolithic carbon aerogel both were synthesized at the same sol–gel pH. Electrochemical measurements were performed in two electrode Swagelok-type cells, using lithium as a counter electrode. The typical mass and volume of C/TiO_2 monolith electrode were $\sim$2 mg and $\sim$13.5 mm^3, respectively. The loading density was $\sim$22.2 mg cm^{-2}. The first discharge curves of the hybrid (red line) and carbon (black line) aerogel electrodes at a rate of 1C (168 mA g^{-1} calculated based on properties of TiO_2) are shown in Fig. 5, as well as those after 10 charge–discharge cycles in dotted lines. Here, we define the scan rate of 1C based on the theoretical capacity of TiO_2 (anatase), which is 168 mAh g^{-1}, by the reaction, $TiO_2 + 0.5Li \leftrightarrow Li_{0.5}TiO_2$, [52]. In addition, this scan rate of 168 mA g^{-1} was used to compare the capacity of the TiO_2 component in the hybrid co-aerogel to that of TiO_2 in other hybrid nanocomposites where carbon nanotubes or graphene were mixed to enhance their capacity [36–39].

The standard measurement parameters for either TiO_2 materials and for carbon materials cannot be directly used because the hybrid co-aerogel is composed of 58.2 wt% of TiO_2 and 41.8 wt% of carbon as analyzed by TGA, shown in the supporting information. Therefore, in order to take the contribution from the carbon component into full account, we have studied the Li^+ insertion/desertion over larger voltage range, 3.0–0.05 V vs. Li^+/Li. This measurement method was used to provide more complete information of the composite materials made from CNT and TiO_2 in earlier publications [54]. As shown in Fig. 5, in the discharge curve of the hybrid

Fig. 4. (a) The diameter contribution of TiO$_2$ nanoparticles in the hybrid co-aerogels under different pH at 1.08, 1.20 and 1.39. Error bars represent the standard deviation calculated from the diameter distributions of each samples. X-axis is the sol−gel pH (measured by accumet® AB15 + Basic pH/mV Benchtop Meter) and Y-axis is the diameter distribution in nm (measured by high-resoluion TEM). (b) The C/TiO$_2$ ratio (wt%) effect on the BET surface area. X-axis is TiO$_2$/carbon weight ratio (wt.%) and Y-axis is surface area in m^2 g^{-1}.

co-aerogel, the potential decreases quickly from the open-circuit voltage down to a value of ∼1.75 V vs. Li$^+$/Li. Then, the voltage plateau corresponding to the Li$^+$ insertion/desertion in TiO$_2$ was clearly visible around 1.75 V vs. Li$^+$/Li. After the plate plateau region, the gradual decay of the voltage was observed. It is worthwhile to note that, in the voltage range of 3.0−0.05 V vs. Li$^+$/Li, the total first-discharge capacity of the hybrid electrode (648.7 mAh g^{-1}) was much higher than that of the reference carbon electrode (214.9 mAh g^{-1}), as shown in Fig. 5. This superior performance is accredited to two different Li storage mechanism in the TiO$_2$ and carbon components. The 3D-interconnected porous nature of the TiO$_2$ component in the hybrid co-aerogel allows fast ion diffusion. The Nyquist plot in Fig. 9 reveals that the charge transfer resistance (R_{ct}) and the Warburg conductivity (σ_W) of the hybrid co-aerogel are lower and higher than that of the reference carbon electrode, respectively. More details about impedance analysis will be discussed later. More interestingly, we believe that the nanosized TiO$_2$ component in the hybrid co-aerogel enhances surface storage mechanism (pseudo-capacities) resulting in the superior lithium storage capability at the potential lower than 1.75 V vs. Li$^+$/Li. Jiang et al. reported the surface storage mechanism of TiO$_2$ NPs where the electrode made from a very fine anatase TiO$_2$ NPs of 6 nm exhibited the higher capacity than that of larger TiO$_2$ NPs even at high current rates [55]. Their result indicates further insertion of the lithium ions into the surface layer of the electrode material. The same trend was observed in our experiment. Fig. 7 shows the relative capacity ratio between the hybrid and carbon
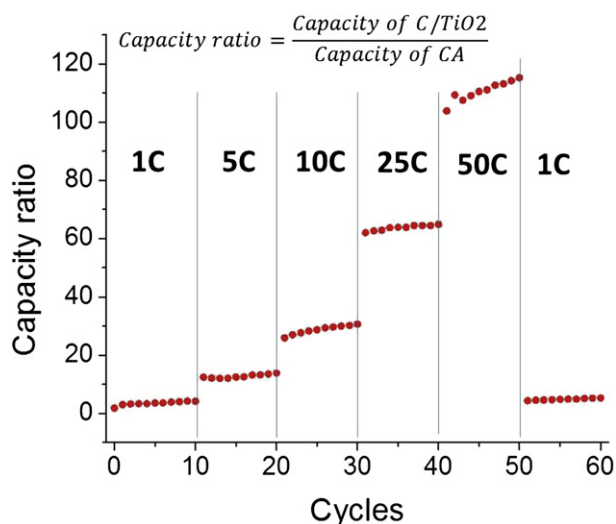
aerogels, which is calculated by dividing the capacity of the hybrid co-aerogels by that of carbon aerogels at different scan rates. X-axis is scan rate in C and Y-axis is capacity ratio without unit. It is obvious that the higher the current density, the better the cycling performance of the hybrid co-aerogels than that of the reference carbon aerogels. Fig. 8 shows the 10th galvanostatic charge and discharge curves of the hybrid co-aerogel synthesized at 1.20 sol−gel pH (∼7 nm TiO$_2$ NPs) and those of a hybrid co-aerogel synthesized at 1.39 sol−gel pH (∼10 nm TiO$_2$ NPs). The scanning rate was 5C (=840 mA g^{-1}). It is clear that smaller TiO$_2$ NPs network (7 nm) results in higher discharge capacity compared to that of larger TiO$_2$ NPs network (10 nm) lower than 1.75 V vs. Li$^+$/Li. As explained above, the lower pH leads to the smaller TiO$_2$ NPs network. Figure S7 also shows that a hybrid co-aerogel synthesized at 1.08 sol−gel pH (5.5 nm) exhibits similar discharge capacity of the hybrid co-aerogel synthesized at 1.20 sol−gel pH, but no hybrid co-aerogel can be synthesized lower than 1.08 sol−gel pH. In addition, as shown in Fig. 9, the high electrical conductivity of the 3D-interconnected carbon network facilitates fast electron transport to the TiO$_2$ NPs, which has low conductivity that can limit its charge/discharge rate. Furthermore, the 3D-interconnected carbon network will also act as additional lithium storage sites, leading to a dual mechanism of lithium storage. Besides, as mentioned above, the actual surface area of the carbon component in the hybrid co-aerogel (915 m^2 g^{-1}) is much higher than that of the carbon
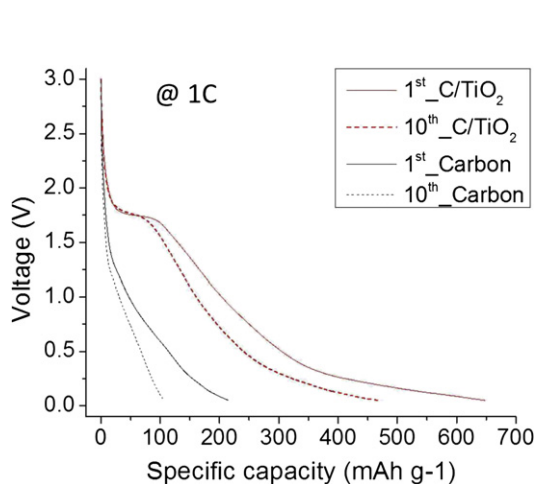
Fig. 5. The 1st and 10th galvanostatic discharge curves of the hybrid co-aerogel at a rate of 1C (=168 mA g^{-1}) and compared to that of the reference carbon aerogel.
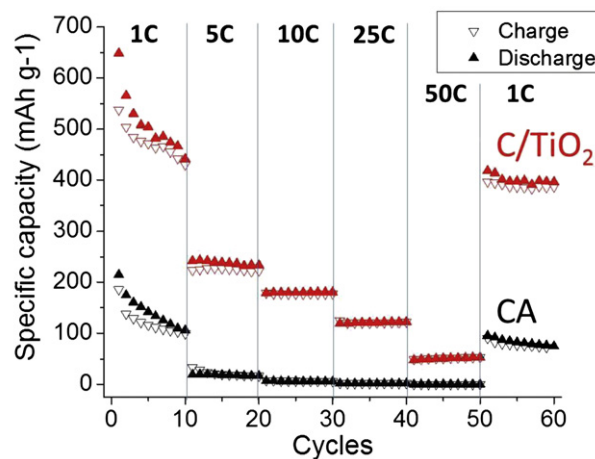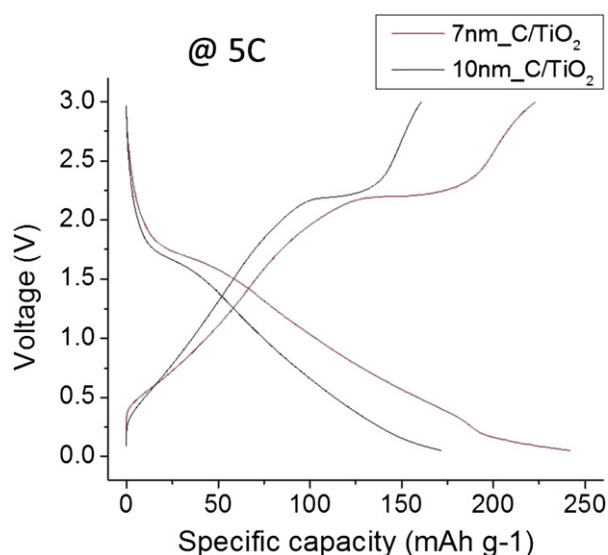

Fig. 6. Scan rate performance of the hybrid co-aerogel (from 1C to 50C, then back to 1C) compared to that of the carbon aerogel. X-axis is the number of cycles and Y-axis is the specific capacity in mAh g^{-1}.
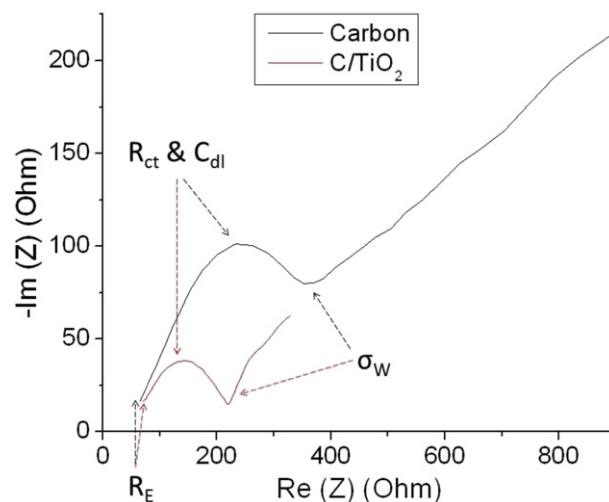
Fig. 7. Relative capacity ratio between the hybrid and carbon aerogels, which is calculated by dividing the capacity of the hybrid co-aerogels by that of carbon aerogels at different scan rates.

Fig. 9. Nyquist plots of the electrodes of the hybrid (red) and the carbon aerogels (black). All of the measurements were conducted using a voltage window of 3.0–0.05 V vs. Li^+/Li.(For interpretation of the references to colour in this figure legend, the reader is referred to the web version of this article.)

aerogel (657 m^2 g^{-1}), resulting in higher capacity of the hybrid co-aerogel than that of the carbon aerogel.

Figure S6 in the supporting information shows the capacity comparison between the hybrid co-aerogel and the carbon aerogel electrodes in the smaller voltage range of 3.0–1.0 V vs. Li^+/Li. The hybrid co-aerogel showed a capacity of 203.9 mAh g^{-1}, which is comparable to the recent developments where expensive carbon materials, such as CNTs and graphene, were mixed with TiO_2 [36–39]. The capacity of 203.9 mAh g^{-1} was higher than the theoretical value of 168 mAh g^{-1} for TiO_2 materials. However, such values were observed in earlier reports and attributed to the high insertion coefficient for the first cycle, the surface storage mechanism (pseudo-capacities) and possible contribution from carbon materials [56,57]. As clearly shown in Figure S6 in the supporting information, the capacity contribution from carbon component in the hybrid co-aerogel cannot be neglected.

Fig. 8. The 10th galvanostatic charge and discharge curves of the hybrid co-aerogel synthesized at 1.20 sol–gel pH (∼7 nm TiO_2 NPs) and compared to that of a hybrid co-aerogel synthesized at 1.39 sol–gel pH (∼10 nm TiO_2 NPs). The scanning rate was 5C (= 840 mA g^{-1}).

Fig. 5 also shows that the discharge capacities of the hybrid co-aerogel (red dotted) and the carbon aerogel (black dotted) after 10 cycles were 466.7 mAh g^{-1} and 106.6 mAh g^{-1}, respectively. These capacity values showed that, after 10 cycles, the hybrid co-aerogel and the carbon aerogel showed irreversible capacity losses of 28.1% and 50.4%, respectively. In other words, the capacity of the carbon aerogel diminished much faster than that of the hybrid co-aerogel. This trend was also observed in the charge/discharge test at various current rates, discussed next.

The rate capability of the hybrid co-aerogel as electrode for Li-ion battery was then evaluated by charge/discharge test at various charging rates from 1C to 50C, as shown in Fig. 6, and compared to that of the reference carbon aerogel. The values for capacities were obtained in a voltage range 3.0–0.05 V vs. Li^+/Li. It is clear that the hybrid co-aerogel shows higher cyclic discharge-capacity at each rate than that of the carbon aerogel. Notably, a discharge-capacity of 399 mAh g^{-1} (This value is 138 mAh g^{-1} if the capacity is measured in a voltage window of 3.0–1.0 V vs. Li^+/Li) can be resumed and stabilized when the current rate is reduced back to 1C, suggesting the good mechanical stability of the hybrid co-aerogel as a monolithic anode. As mentioned above, it is worthwhile noting that the higher the current density, the better the cycling performance of the hybrid co-aerogels compared to that of the reference carbon aerogels, as clearly shown in Fig. 7.

Fig. 9 shows the Nyquist plots comparison (after 60 charge–discharge cycles) between the hybrid and carbon co-/aerogels. The composite electrode model proposed by Troltzsch et al. was used for interpretation. The measurement frequency lies between 0.1 Hz and 100 kHz. As shown in Fig. 9, the series resistances (R_E) of the hybrid and carbon electrodes are similar, indicating that there was no reduction of conductivity in the hybrid co-aerogels by adding TiO_2 NPs. The 3-D interconnected nanostructure of the carbon component inside the hybrid co-aerogel maintains conductivity equivalent to that of the reference carbon aerogel. In addition, the impedance spectrum of the reference carbon aerogel shows that the transition between charge transfer semicircle and diffusion spike became softer than that of the hybrid co-aerogel. It means that the Warburg conductivity (σ_W) of the reference carbon aerogel is lower than that of the hybrid co-aerogels, indicating lower diffusion coefficient and lithium concentration in the reference carbon aerogel. Furthermore, the charge transfer resistance

(R_{ct}) of the reference carbon electrode is significantly higher than that of the hybrid co-aerogel. This indicates that the exchange current density of the reference carbon aerogel is lower than that of the hybrid co-aerogel.

3. Conclusions

In summary, we have developed a convenient, inexpensive and scalable method to synthesize carbon (resorcinol-formaldehyde) and TiO_2 co-gel and co-aerogel. It is found that the solvent choice, catalyst and pH are critical factors to obtain uniform and stable hybrid inorganic/organic co-gels and co-aerogels. By using the carbon and TiO_2 co-gel, the hybrid co-aerogel was prepared and characterized. The results demonstrate that both the carbon and the TiO_2 components possess a 3-D interconnected nanostructure. In addition, the diameter of TiO_2 NPs in the hybrid co-aerogel can easily controlled by the pH. Interestingly, it is also found that TiO_2 network is wrapped by carbon network, resulting in the increase of BET surface area of the carbon aerogel after removing TiO_2 component by HF treatment. The hybrid co-aerogel proves its superior potential as an anode of LIBs compared to that of the reference carbon aerogel using the galvanostatic charge–discharge test and to other TiO_2/carbon composites in earlier literature [25–27,32,37–39,54]. Two plate plateaus were found (around 1.75 V and below 1.0 V) and caused by Li^+ insertion to the TiO_2 and carbon components of the hybrid co-aerogel, respectively. It is found that the higher the current density, the better the cycling performance of the hybrid co-aerogel than that of carbon aerogel due to the surface storage mechanism (pseudo-capacities). Moreover, the impedance plots reveal no reduction of the conductivity of the hybrid co-aerogels due to the 3-D interconnected nanostructure of the carbon component. The impedance plots also demonstrate lower internal resistance of the hybrid co-aerogel than that of the carbon aerogel. In this report, we synthesized the hybrid co-aerogel and demonstrated high capacity, good rate performance and superior stability as an anode electrode material in LIBs. We believe these results demonstrated the potential of the co-aerogel approach as electrode materials for energy storage. It has the potential to be applied to many other metal oxide systems for broader applications. Such research projects are on-going in our research lab.

4. Experimental section

Hybrid co-aerogels synthesis: For carbon aerogels precursors, predetermined amounts of resorcinol (R) (Sigma Aldrich, ACS reagent, ≥99.0%), formaldehyde (F) (ACROS, ACS reagent, 37 wt% sol., stab. 10–15% methanol) and sodium bicarbonate (S) (ACROS, 99.6%, ACS reagent) were mixed in an appropriate amount of ethanol (E) (VWR, Ethanol, 200 proof, KOPTEC) at room temperature. The molar ratio of R/E, R/F and R/S were 0.0524, 0.5 and 200. A bath sonication was used to make homogeneous solution. For titanium dioxide aerogels precursors, predetermined amount of titanium (IV) isopropoxide (Ti) (Sigma Aldrich, 97%) was added in an appropriate amount of ethanol at room temperature and the molar ratio of Ti/E was 0.05. In a glass vial (20 cm^3 capacity), 5 ml of the RF solution was added followed by adding 1.45 g of HCl solution (1.5 M) and lastly adding 5 ml of the Ti solution. The mixture of acid added RF solution and Ti solution became a gel within 30 min accredited to the gelation of TiO_2. Then, we sealed the vial and then placed it in an oven at 70 ± 2 °C for 12 h for the gelation of resorcinol and formaldehyde. Subsequently, the hybrid organic/inorganic gel was dried by critical point dryer (CPD from Bal-Tec) using CO_2. The dried hybrid gel was carbonized with a quartz tube furnace at 900 °C at a heating rate of 10 °C min^{-1} for 5 h under

argon (Ar) and hydrogen (H_2) atmosphere (Ar and H_2 flow rate=800 mL min^{-1} and 80 mL min^{-1}).

Characterization: SEM and TEM images were obtained on a FEI/Phillps XL30 ESEM-FEG and Tecnai™ G2. The diameters of TiO_2 NPs were measured by using TEM images. Moreover, XRD patterns of the samples were acquired on PANalytical X'Pert PRO MRD high-resolution diffractometer with Cu Kα radiation. In addition, XPS spectrum was measured by Kratos Analytical Axis Ultra. In order to calculate BET surface area of the samples, nitrogen adsorption–desorption isotherm measurements were conducted at 77 K with Micromeritics TriStar 3000. TGA spectra (TA Instruments SDT 2960) was used to analyze the mass percentage of TiO_2 in the hybrid co-aerogels at a heating rate of 5.0 °C min^{-1}–900.0 °C in air.

Electrochemical measurements: the electrochemical properties of the hybrid co-aerogels as anode materials in lithium ion batteries were evaluated by a galvanostatic charge/discharge technique using BioLogic SP-300. The Swagelok-type cells were assembled in an Ar-filled glove box as shown in Figure S8 in supporting information. Metallic lithium was used as the counter/reference electrode and the monolith of the hybrid co-aerogel was directly used as the working electrode without adding any additives such as carbon black and conducting polymers. 1 M of $LiPF_6$ in the mixture of ethylene carbonate (EC), dimethyl carbonate (DMC) and diethyl carbonate (DEC) in 1:1:1 w/w ratio was used as working electrolyte. The charge/discharge performance was conducted between 3.0–0.05 V vs Li^+/Li and the scan rates were calculated based on the theoretical capacity of an anatase TiO_2 which is 168 mAh g^{-1}.

Appendix A. Supporting information

Supplementary data related to this article can be found online at http://dx.doi.org/10.1016/j.jpowsour.2012.06.070.

References

[1] V. Etacheri, R. Marom, R. Elazari, G. Salitra, D. Aurbach, Energy & Environmental. Science 4 (2011) 3243–3262.
[2] P.G. Bruce, B. Scrosati, J.M. Tarascon, Angewandte Chemie International Edition 47 (2008) 2930–2946.
[3] B. Kang, G. Ceder, Nature 458 (2009) 190–193.
[4] Y. Wang, Y. Wang, E. Hosono, K. Wang, H. Zhou, Angewandte Chemie International Edition 47 (2008) 7461–7465.
[5] N. Li, C.J. Patrissi, G. Che, C.R. Martin, Journal of The Electrochemical Society 147 (2000) 2044–2049.
[6] P.L. Taberna, S. Mitra, P. Poizot, P. Simon, J.M. Tarascon, Nature Materials 5 (2006) 567–573.
[7] L.J. Fu, H. Liu, C. Li, Y.P. Wu, E. Rahm, R. Holze, H.Q. Wu, Solid State Sciences 8 (2006) 113–128.
[8] C.K. Chan, H. Peng, G. Liu, K. McIlwrath, X.F. Zhang, R.A. Huggins, Y. Cui, Nature Nanotechnology 3 (2008) 31–35.
[9] R. Liu, J. Duay, S.B. Lee, Chemical Communications 47 (2010) 1384–1404.
[10] H. Zhang, X. Yu, P.V. Braun, Nature Nanotechnology 6 (2011) 277–281.
[11] M. Yao, K. Okuno, T. Iwaki, T. Awazu, T. Sakai, Journal of Power Sources 195 (2010) 2077–2081.

[12] T. Ripenbein, D. Golodnitsky, M. Nathan, E. Peled, Journal of Applied Electrochemistry 40 (2009) 435–444.
[13] J. Guo, C. Wang, Chemical Communications 46 (2010) 1428–1430.
[14] A.E. Fischer, K.A. Pettigrew, D.R. Rolison, R.M. Stroud, J.W. Long, Nano Letters 7 (2007) 281–286.
[15] N.S. Ergang, J.C. Lytle, K.T. Lee, S.M. Oh, W.H. Smyrl, A. Stein, Advanced Materials 18 (2006) 1750–1753.
[16] N.S. Ergang, M.A. Fierke, Z. Wang, W.H. Smyrl, A. Stein, Journal of The Electrochemical Society 154 (2007) A1135.
[17] J.W. Long, D.R. Rolison, Accounts of Chemical Research 40 (2007) 854–862.
[18] A. Rumplecker, F. Kleitz, E.-L. Salabas, F. Schüth, Chemistry of Materials 19 (2007) 485–496.
[19] Zhou Yue, Chemistry of Materials 19 (2007) 2359–2363.
[20] Y. Wang, H.C. Zeng, J.Y. Lee, Advanced Materials 18 (2006) 645–649.
[21] J. Chen, L. Xu, W. Li, X. Gou, Advanced Materials 17 (2005) 582–586.
[22] L.F. Nazar, G. Goward, F. Leroux, M. Duncan, H. Huang, T. Kerr, J. Gaubicher, International Journal of Inorganic Materials 3 (2001) 191–200.
[23] S.A. Needham, G.X. Wang, H.K. Liu, Journal of Power Sources 159 (2006) 254–257.
[24] M.N. Obrovac, R.A. Dunlap, R.J. Sanderson, J.R. Dahn, Journal of The Electrochemical Society 148 (2001) A576–A588.
[25] B.J. Landi, M.J. Ganter, C.D. Cress, R.A. DiLeo, R.P. Raffaelle, Energy & Environmental Science. 2 (2009) 638–654.
[26] Y. Sun, Q. Wu, G. Shi, Energy & Environmental Science 4 (2011) 1113–1132.
[27] H. Zhang, G. Cao, Y. Yang, Energy & Environmental Science 2 (2009) 932–943.
[28] A.R. Armstrong, G. Armstrong, J. Canales, R. García, P.G. Bruce, Advanced Materials 17 (2005) 862–865.
[29] Y.-M. Lin, P.R. Abel, D.W. Flaherty, J. Wu, K.J. Stevenson, A. Heller, C.B. Mullins, The Journal of Physical Chemistry C 115 (2011) 2585–2591.
[30] A. Fujishima, X. Zhang, D.A. Tryk, Surface Science Reports 63 (2008) 515–582.
[31] B. O'Regan, M. Gratzel, Nature 353 (1991) 737–740.
[32] C. Wang, L. Yin, L. Zhang, R. Gao, Journal of Physics Chemistry C 114 (2010) 4408–4413.
[33] T. Ohzuku, T. Kodama, T.Hirai, Journal of Power Sources, 14 153–166.
[34] E. Peled, Journal of The Electrochemical Society 126 (1979) 2047–2051.
[35] G.-A. Nazri, G. Pistoia, Lithium Batteries: Science and Technology, Springer, 2003.
[36] N. Li, G. Liu, C. Zhen, F. Li, L. Zhang, H.M. Cheng, Advanced Functional Materials 21 (2011) 1717–1722.
[37] S. Ding, J.S. Chen, D. Luan, F.Y.C. Boey, S. Madhavi, X.W. Lou, Chemical Communications 47 (2011) 5780.
[38] F.-F. Cao, Y.-G. Guo, S.-F. Zheng, X.-L. Wu, L.-Y. Jiang, R.-R. Bi, L.-J. Wan, J. Maier, Chemistry of Materials 22 (2010) 1908–1914.
[39] Z. Yang, G. Du, Z. Guo, X. Yu, Z. Chen, T. Guo, H. Liu, Journal of Materials Chemistry 21 (2011) 8591.
[40] M. Wu, Y. Jin, G. Zhao, M. Li, D. Li, Environmental Science and Technology. 44 (2010) 1780–1785.
[41] L. Zou, G. Morris, D. Qi, Desalination 225 (2008) 329–340.
[42] Y. Ishii, Y. Kanamori, T. Kawashita, I. Mukhopadhyay, S. Kawasaki, Journal of Physics and Chemistry of Solids 71 (2010) 511–514.
[43] L.J. Fu, H. Liu, H.P. Zhang, C. Li, T. Zhang, Y.P. Wu, H.Q. Wu, Journal of Power Sources 159 (2006) 219–222.
[44] R. Liu, Y. Ren, Y. Shi, F. Zhang, L. Zhang, B. Tu, D. Zhao, Chemistry of Materials 20 (2007) 1140–1146.
[45] F.J. Maldonado-Hódar, C. Moreno-Castilla, J. Rivera-Utrilla, Applied Catalysis A: General 203 (2000) 151–159.
[46] C.J. Brinker, G.W. Scherer, Sol-Gel Science: The Physics and Chemistry of Sol-Gel Processing, Academic Press, 1990.
[47] Y.S. Hu, P. Adelhelm, B.M. Smarsly, S. Hore, M. Antonietti, J. Maier, Advanced Functional Materials 17 (2007) 1873–1878.
[48] S.A. Al-Muhtaseb, J.A. Ritter, Advanced Materials 15 (2003) 101–114.
[49] J.E. Krzanowski, R.E. Leuchtner, Journal of the American Ceramic Society 80 (1997) 1277–1280.
[50] J. Luthin, C. Linsmeier, Physica Scripta T 91 (2001) 134.
[51] Y.-H. Chang, H.-T.Chiu, Journal of Materials Research, 17 2779-2782.
[52] G. Nuspl, K. Yoshizawa, T. Yamabe, Journal of Materials. Chemistry 7 (1997) 2529–2536.
[53] S.L. Isley, R.L. Penn, The Journal of Physical Chemistry C 112 (2008) 4469–4474.
[54] S. Ding, J.S. Chen, X.W. Lou, Advanced Functional Materials 21 (2011) 4120–4125.
[55] C. Jiang, M. Wei, Z. Qi, T. Kudo, I. Honma, H. Zhou, Journal of Power Sources 166 (2007) 239–243.
[56] J.S. Chen, Y.L. Tan, C.M. Li, Y.L. Cheah, D. Luan, S. Madhavi, F.Y.C. Boey, L.A. Archer, X.W. Lou, Journal of the American Chemical Society 132 (2010) 6124–6130.
[57] H.-W. Shim, D.K. Lee, I.-S. Cho, K.S. Hong, D.-W. Kim, Nanotechnology 21 (2010) 255706.